Steady-State Deformation of the Coso Range, East-Central California, Inferred from Satellite Radar Interferometry

Charles W. Wicks[1] (cwicks@usgs.gov)
Wayne Thatcher[1] (thatcher@usgs.gov)
Francis C. Monastero[2] (MonasteroFC@navair.navy.mil)
Michael A. Hasting[2] (HastingMA@navair.navy.mil)

[1] US Geological Survey, 345 Middlefield Rd — MS 977, Menlo Park, CA 94025

[2] Geothermal Program Office, NAWS, China Lake, CA 93555

Abstract

Observations of deformation from 1992-1997 in the southern Coso Range using satellite radar interferometry show deformation rates of up to 35 mm/yr in an area ~10 km by 15 km. The deformation is most likely the result of subsidence in an area around the Coso geothermal field. The deformation signal has a short wavelength component, related to production in the field, and a long wavelength component, deforming at a constant rate, that may represent a source of deformation deeper than the geothermal reservoir. We have modeled the long wavelength component of deformation and inferred a deformation source at ~ 4 km depth. The source depth is near the brittle-ductile transition depth (inferred from seismicity) and ~1.5 km above the top of the rhyolite magma body that was a source for the most recent volcanic eruption in the Coso volcanic field (*Manley and Bacon*, 2000). From this evidence and results of other studies in the Coso Range, we interpret the source to be a leaking deep reservoir of magmatic fluids derived from a crystalizing rhyolite magma body.

Introduction

The Coso Range is located on the western edge of the Eastern California Shear Zone (ECSZ) —locally, a broad transitional zone of distributed shear that accommodates ~20-25% of the Pacific plate-North American plate differential motion. Panamint Valley and Death Valley (Figure 1), both within the ECSZ, contain Basin and Range type of normal fault deformation and right-lateral strike-slip faults related to the transform motion between the North American and Pacific plates (e.g. *Hearn and Humphreys*, 1998). The seismically active Coso Range also contains these two styles of deformation in addition to left-lateral strike-slip faults. The landscape of the southern Coso Range is dominated by the domes, cinder cones and lava flows of the Coso Volcanic field that formed during three major episodes of volcanism that began ~6 million years (Ma) ago in the northern Coso Range *(Novak and Bacon*, 1986).

Novak and Bacon (1986) used the compositional evolution of the Plio-Pleistocene volcanics and observed relations of the volcanics with mapped faults to construct a history of the tectonic evolution of the Coso Range. They showed that during the first Pliocene eruptions ~4 Ma, basalt was erupted into a shallow depression lacking much relief, most likely under conditions of little if any, crustal extension. Subsequent Pliocene magmas became increasingly silicic as the area entered an extensional regime. Normal faulting began ~3 Ma with accompanying uplift and WNW-ESE extension that dissected many of the previously erupted basalt flows with NNE striking normal faults, forming the Coso Basin. Features of the eruption history considered together with the minor amount of contemporaneous pyroclastic activity and petrographic features of the Pleistocene rhyolites led *Bacon et al*.(1981) and *Bacon* (1982) to conclude that the Coso Volcanic field is a tectonically leaking magmatic system . In such a system extensional strain accumulates in the roof rocks at a near constant rate allowing ascending magma to leak volatiles, thus preventing large pyroclastic eruptions.
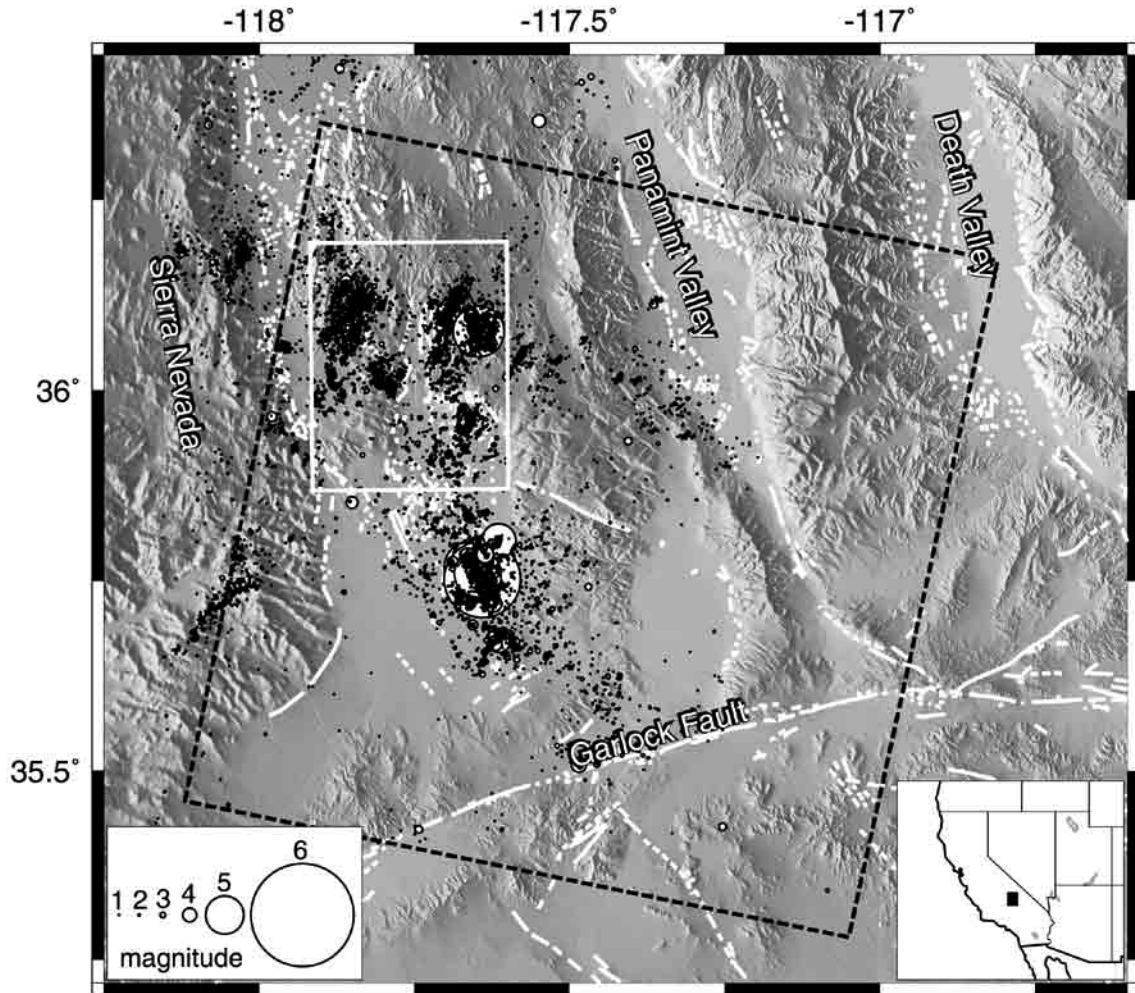
Figure 1 Regional relief map of the Coso area from 90m USGS DEM. White box shows study area of the southern Coso Range. Box with black dashed border shows approximate outline of satellite radar scenes used in this study. Faults from *Jennings* (1975) are shown in white. Earthquakes ‡ 1.0 magnitude recorded by the Southern California Seismic Network relocated by Haukkson (2000) are shown as black circles with white fill. The inset in the lower right shows the location of this regional map in the western United States.

    Bacon et al. (1980) found the orientation of the faults and volcanic vents in the basin to be consistent with the extension direction found in seismo-tectonic studies. *Weaver and Hill* (1979) proposed that the Coso volcanic field is presently an area of local spreading with near E-W extension centered on the geothermal area (Figure 2). Subsequent seismic studies (*Walter and Weaver,* 1980*; Feng and Lees,* 1998) reported dominantly normal fault events in the geothermal area. The direction of the maximum extensional strain rate (N 73°W) in the ECSZ immediately north of Coso Basin derived

from Global Positioning System (GPS) data (*Gan et al.,* 2000) is consistent with the least compressive stress orientation inferred from geologic and seismic data. Monastero et al. (1997) provided data that supported the idea that the Coso geothermal area is a nascent metamorphic core complex forming in a releasing bend setting. This north-northwest trending strike-slip fault zone, that includes the Airport Lake fault zone of Indian Wells Valley, is actively accommodating up to 5 mm/yr of right-lateral offset (King et al., 1998).

A hydrothermal system has been active within the volcanic field for the last ~0.3 Ma (*Bacon*, 1982) and it is related to the last Pleistocene volcanic episode that lasted from ~0.3 to ~0.04 Ma (*Bacon,* 1982). The geothermal potential of the area was first realized in the 1980 s with production beginning in 1987 and development continuing to today. The Coso geothermal field, largely contained within the China Lake Naval Weapons Center, is currently one of the largest producers of geothermal energy in the United States. Fluids extracted from the geothermal reservoir at the wells are injected back into the reservoir.

Several lines of evidence suggest active deformation is currently localized in the Coso Range. These include the presence of 1) an active magmatic system beneath Coso, 2) an active geothermal system, and 3) a high rate of seismicity. Furthermore, GPS studies have reported anomalous horizontal deformation of up to 20 mm/yr near the Coso Geothermal Field (*King et al.,* 1998, *Gan et al.,* 2000). In this paper we use satellite radar interferometry (InSAR) to further investigate the surface deformation in the Coso Range. We show that the dry, sparsely vegetated area is an ideal environment for InSAR, permitting us to map the spatial pattern of deformation and determine the extent and geometry of the sources of deformation beneath the Coso Range. In what follows, we first describe the InSAR images of deformation, then model the data with simple equivalent sources and conclude with a discussion of the implications of our results for magmatic/geothermal processes occurring beneath the Coso Range.
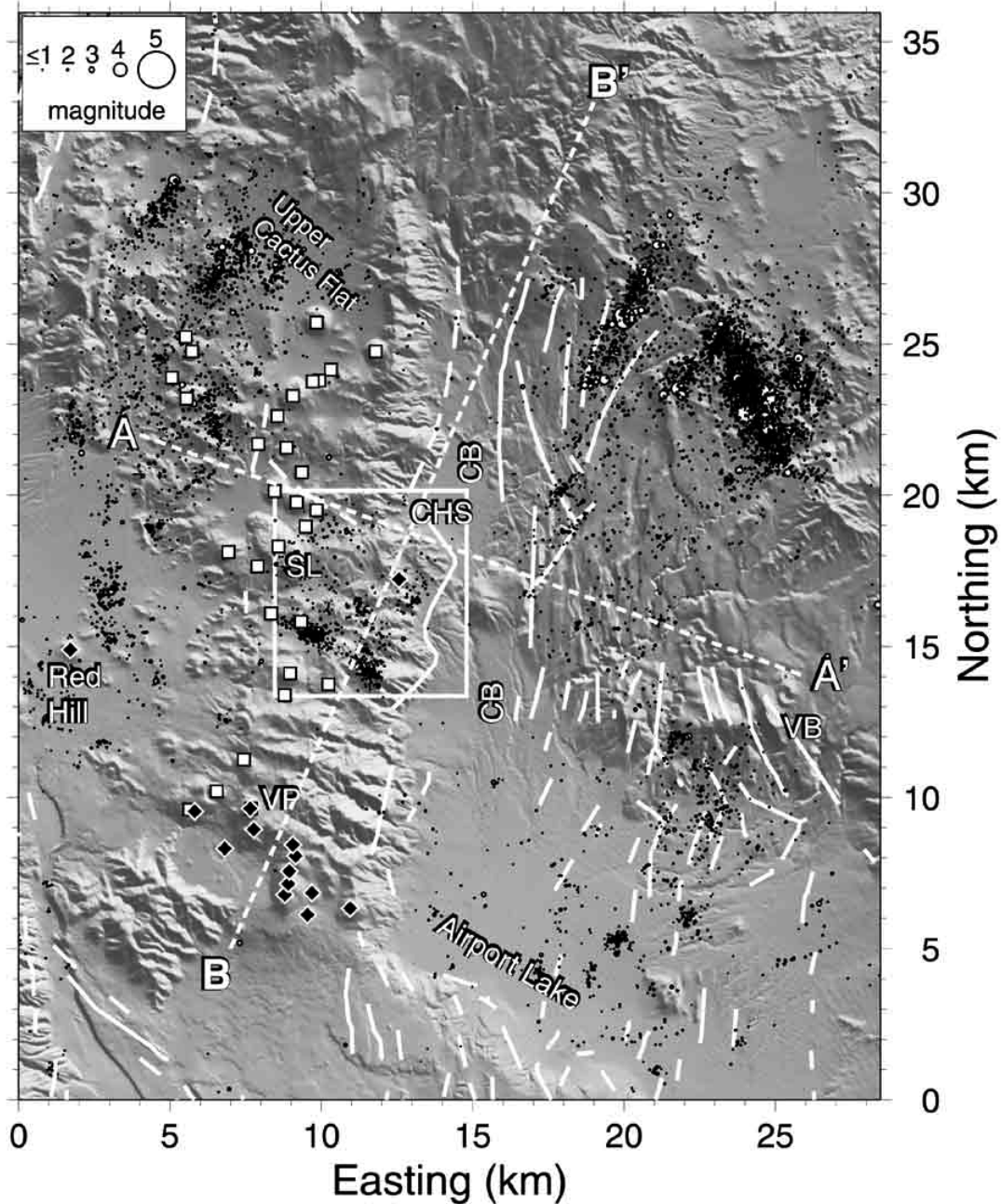
Figure 2 Relief map of study area (UTM projection, coordinates of SW corner are Easting — 417450 m [117.914° W], Northing — 3969600 m [35.869 N])— all interferograms presented cover this same area. The white box roughly outlines the Coso geothermal field. Black circles with white fill show locations of all earthquakes recorded at the Southern California Seismic Network relocated by Haukkson (2000) that occurred within the time spanned by interferograms (92/06/17 to 97/07/05). Faults from *Jennings* (1975) shown in white. Abbreviated geographic features are: CB — Coso Basin, CHS —Coso Hot Springs, SL — Sugar Loaf Mountain, VB — Volcano Butte, VP — Volcano Peak. White filled black squares denote rhyolitic vents younger than 0.3 Ma, black filled white diamonds denote basalitc vents younger than 0.3 Ma (*Duffield et al.,* 1980; *Bacon et al.,* 1980; *Duffield and Bacon,* 1981; *Bacon,* 1982). Dashed lines labeled A-A and B-B show locations of profiles shown in Figs. 5 and 7.

InSAR Obervations

We use European Space Agency (ESA) ERS satellite radar data from 1992 through 1997 to measure deformation in the Coso Range. The satellites emit C-band radar pulses and repeat an orbit every 35 days. The deformation fields for Coso are mapped in interferograms formed using the two-pass method and software developed by Massonnet (*Massonnet et al.,* 1995). Topographic corrections are applied to the interferograms using a 30 meter U. S. Geological Survey (USGS) digital elevation model (DEM) (Figure 2). InSAR measures the change in range (line-of-sight distance) between points on the ground and the satellite position. The satellite unit look vector for the center of Figure 2 is (0.41, -0.08, 0.91) in the direction (east, north, up) with east and north positive -- the range change is thus most sensitive to vertical ground displacement.

Figure 3 shows the extent and pattern of deformation measured in a four-year time interval. Each fringe (cycle of the color table, Figure 3) in the interferogram represents 28.3 mm of range change. The deforming area (~10 km by 15 km) is centered on Coso Basin, with peak deformation rates of up to 35 mm/yr range change indicating broad subsidence surrounding the producing areas of the Coso Geothermal Field. The anomaly is sharply defined on the west, bounded by the Pleistocene volcanic centers that have been active in the last 0.3 Ma, with the exception of a ~0.240 Ma basaltic vent (one of the older vents shown) that lies within the geothermal field (Figure 2). Either the volcanic bodies or faults along which the volcanics were extruded appear to bound the deformation field on the west. There are two apparent wavelengths of deformation: 1). A short wavelength (~2 km) signal within the geothermal field and intimately associated with production and an area of active venting near CHS (Figure 2), and 2) A long-wavelength (10-15km) signal either representing a deeper source of deformation and/or long-term reservoir draw-down
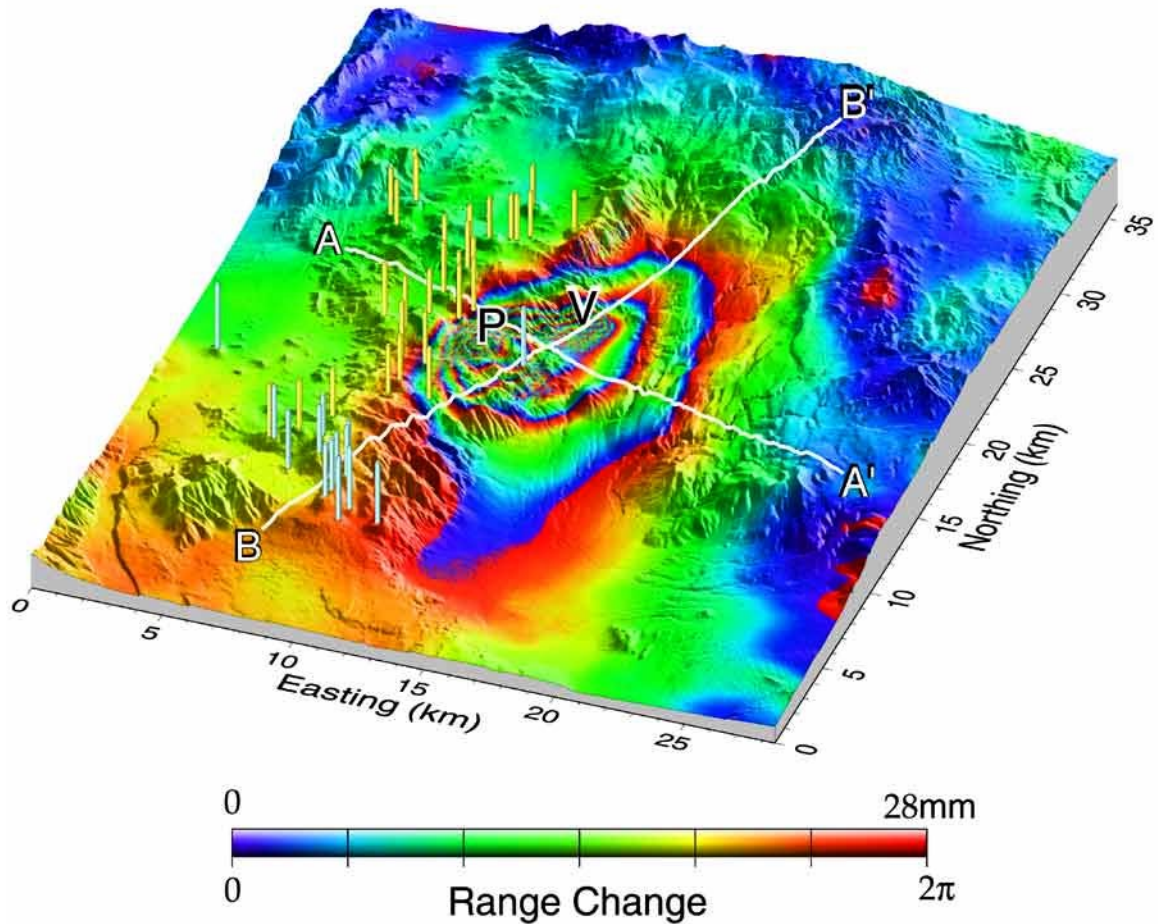
Figure 3 Interferogram for scene pair 92/06/17 to 96/09/28 (Table 1). The interferogram is draped over the 30 m DEM used to apply the topographic correction to the interferogram. Yellow columns denote rhyolitic vents younger than 0.3 Ma, cyan columns denote basaltic vents younger than 0.3 Ma (*Duffield et al.,* 1980; *Bacon et. al.,* 1980; *Duffield and Bacon,* 1981; *Bacon,* 1982). Solid white lines labeled A-A and B-B show locations of profiles shown in Figs. 5 and 7. The letter P indicates the production related short-wavelength anomaly, whereas the letter V indicates a short-wavelength anomaly related to active venting in the vicinity of Coso Hot Springs. The colorbar at the bottom shows the correspondence between color and amount of range change.

To measure changes in the deforming area with time, we have produced five interferograms (Figure 4) made using radar scenes that span more than 24 months between acquisition dates and have orbital separations optimal for interferometry (Table 1). The measure of orbital separation we use is the altitude of ambiguity (h_a): the amount of topography required to produce one interferometric fringe. The pairs with the largest h_a are least affected by elevation errors in the DEM used to correct for topography and thus make the best interferograms.
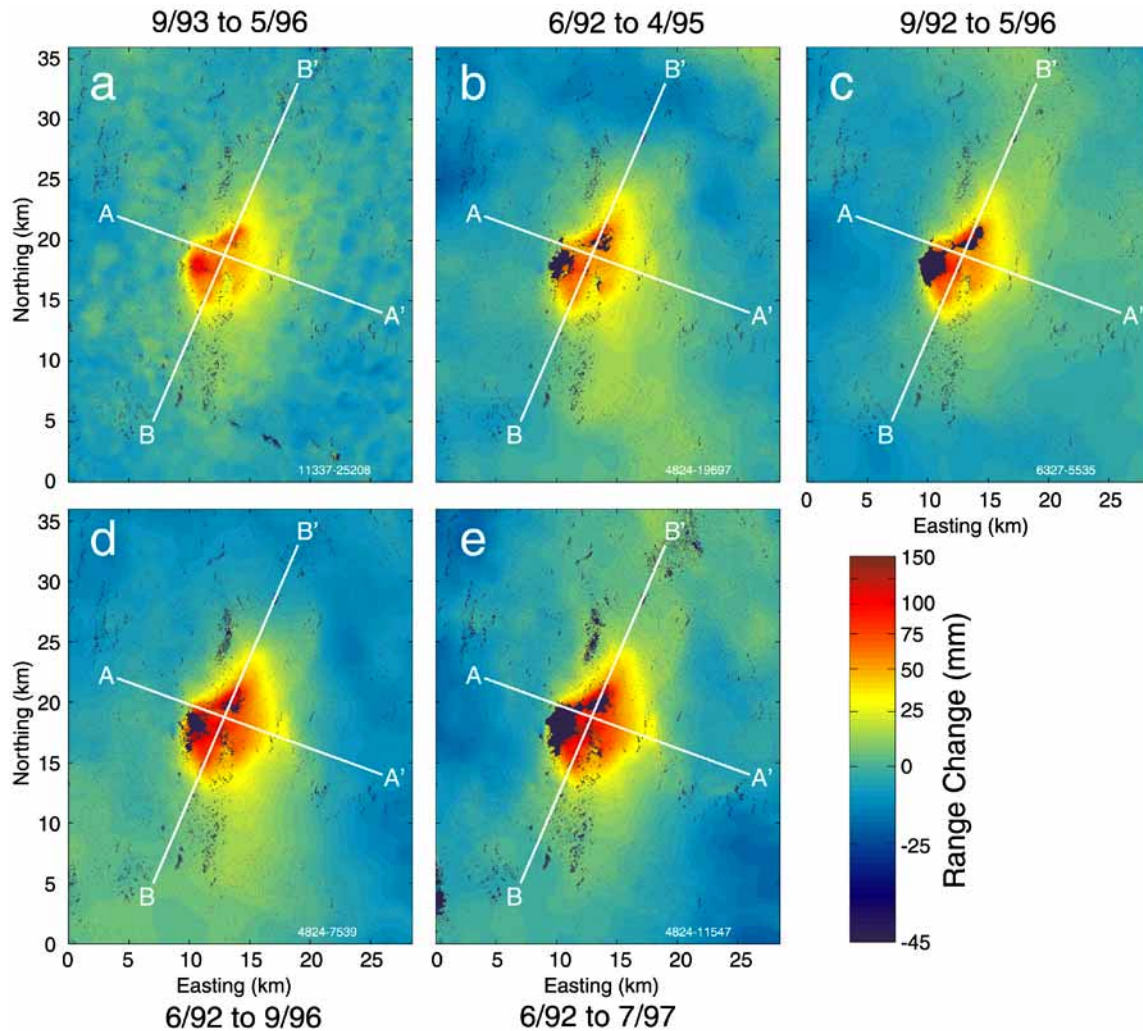
Figure 4 Five unwrapped interferograms in order of increasing amount of time spanned (Table 1). The color bar shows the correspondence between range change and color.Black areas correspond to regions of low coherence. **(a)** ~32 month interferogram from 93/09/15 to 96/05/10, **(b)** ~34 month interferogram from 92/06/17 to 95/04/21, **(c)** ~44 month interferogram from 92/09/30 to 96/05/11, **(d)** ~51 month interferogram from 92/06/17 to 96/09/28, and **(e)** ~61 month interferogram from 92/06/17 to 97/07/05.

The phase of each pixel in an interferogram is a measure of the range change *modulo* 2π between the ground and the satellite. The process of removing the $2n\pi$ uncertainty is called unwrapping, performed here using a branch-cut method (*Goldstein et al.,* 1988). In order to successfully unwrap the interferograms we first filter them using the filtering algorithm of *Goldstein and Werner* (1998). Each interferogram in Figure 4 has been filtered to reduce noise, then unwrapped and scaled to yield displacement in units of mm of range change.

Figure No.	Master Image			Slave Image			h_a (m)	Frame /Track
	Orbit No.	Satellite	Acquisition Date (yr/mo/dy)	Orbit No.	Satellite	Acquisition Date (yr/mo/dy)		
4a	11337	ERS1	93/09/15	25208	ERS1	96/05/10	33700	2885/170
4b	4824	ERS1	92/06/17	19697	ERS1	95/04/21	2698	2885/170
4c	6327	ERS1	92/09/30	5535	ERS2	96/05/11	643	2885/170
3, 4d	4824	ERS1	92/06/17	7539	ERS2	96/09/28	143	2885/170
4e	4824	ERS1	92/06/17	11547	ERS2	97/07/05	73	2885/170

Table 1. The individual satellite images used to construct the five interferograms shown in Figure 4.

The pattern and rate of deformation are remarkably similar from scene to scene in Figs. 4 and 5 implying an underlying process that is steady-state (at least temporarily). Although the range change increases with time, the deformation rate appears to be constant, generally within –4 mm/yr, except in the centers of production within the geothermal field. A comparison of the deformation rate in profiles A-A and B-B (Figure 5) shows the extent of deformation also remains unchanged in 1992-1997.
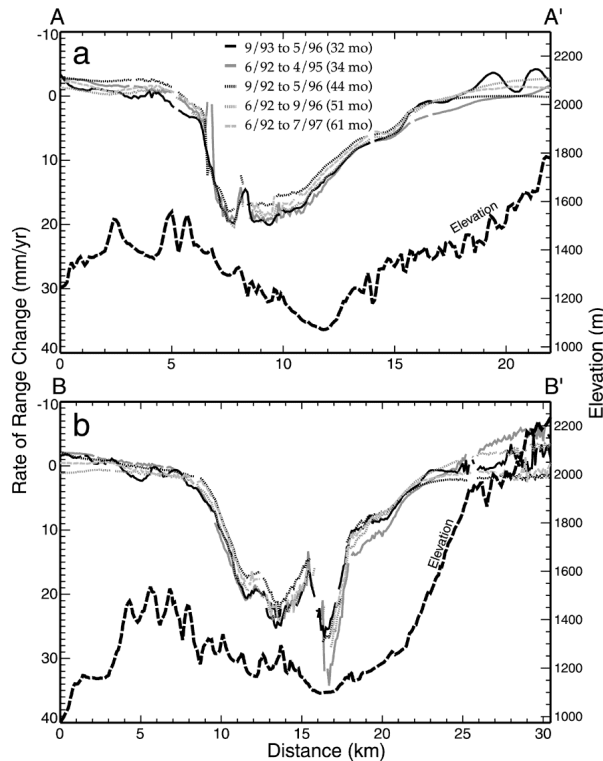

Figure 5 Rate of range change measured on profiles of Figure 4. Elevation on the profiles is shown with the heavy black dashed line in the bottom of each plot. The correspondence between line style and interferogram (Figure 4, Table 1) is shown in the top of Figure 5a. **(a)** Rate of range change along profile A-A , **(b)** Rate of range change along profile of B-B .

Modeling

We focus on using the interferograms in Figure 4 to estimate the depth and geometry of the source of the long-wavelength deformation signal. The short-wavelength deformation peaks are clearly shallow in origin, related to production and active venting (see Figure 3) and fall mostly within the less coherent regions of the images. The loss of coherence probably results from changes in the surface radar scatterers related to operations around the geothermal field. Note that in Figure 4 the size of the area of weak coherence generally increases with the length of the time interval spanned.

To model the long-period signal, we invert for a single equivalent source of deformation. We perform two inversions for each interferogram in Figure 4, one for a conventional buried point source (*Mogi,* 1958) and one for a planar elastic dislocation (*Okada,* 1985). We assume in each case that the source is located in an isotropic homogeneous elastic half-space. We model the data by employing the Levenberg-Marquardt method: a non-linear least squares technique (e.g. *Press et al.,* 1992) that iteratively improves the trial solution until the goodness-of-fit , χ^2, effectively stops decreasing. A Mogi source is described by four model parameters: the x, y location coordinates, the depth, and the volume change. The planar elastic dislocation source is described by eight model parameters: the x, y location coordinates, the depth, the length and width, the amount of movement perpendicular to the dislocation surface, and the strike and the dip of the planar surface. Synthetic interferograms were calculated for the dislocation model using the program RNGCHN written by *Feigl and Dupr* (1999). Initial trials that included the in-plane components of dislocation slip only marginally improved the model fits, so only the perpendicular component was permitted to vary in subsequent inversions.

Because of the elongate signature of the deformation anomaly (Figure 4) the elastic dislocation model proved to be superior to the Mogi model in matching each of the five interferograms. An F-test revealed that the variance of the residual for the elastic dislocation model was lower than the variance of the residual for the point source model at better than 99.9% significance in each of the five cases. In Figure 6 we show the surface projection of the elastic dislocation model that best fits the interferogram in Figure 4a. The model projection is plotted on a synthetic interferogram generated from

the best-fit model and on the residual interferogram. The residual interferogram shows that the long wavelength signal is modeled very well. Note that the unmodeled short-wavelength signal falls almost entirely within the geothermal field (Figs. 2, 6). In Figure 7 we compare calculated and observed range change values along profiles A-A and B-B for three independent interferograms (interferograms without common scenes). The comparison again shows that the long wavelength signal is well modeled, while the short wavelength production signal is not. The sharp peaks in the data between 15 and 17 km along profile B-B result from active venting near CHS (Figure 2) in the north end of the geothermal field.
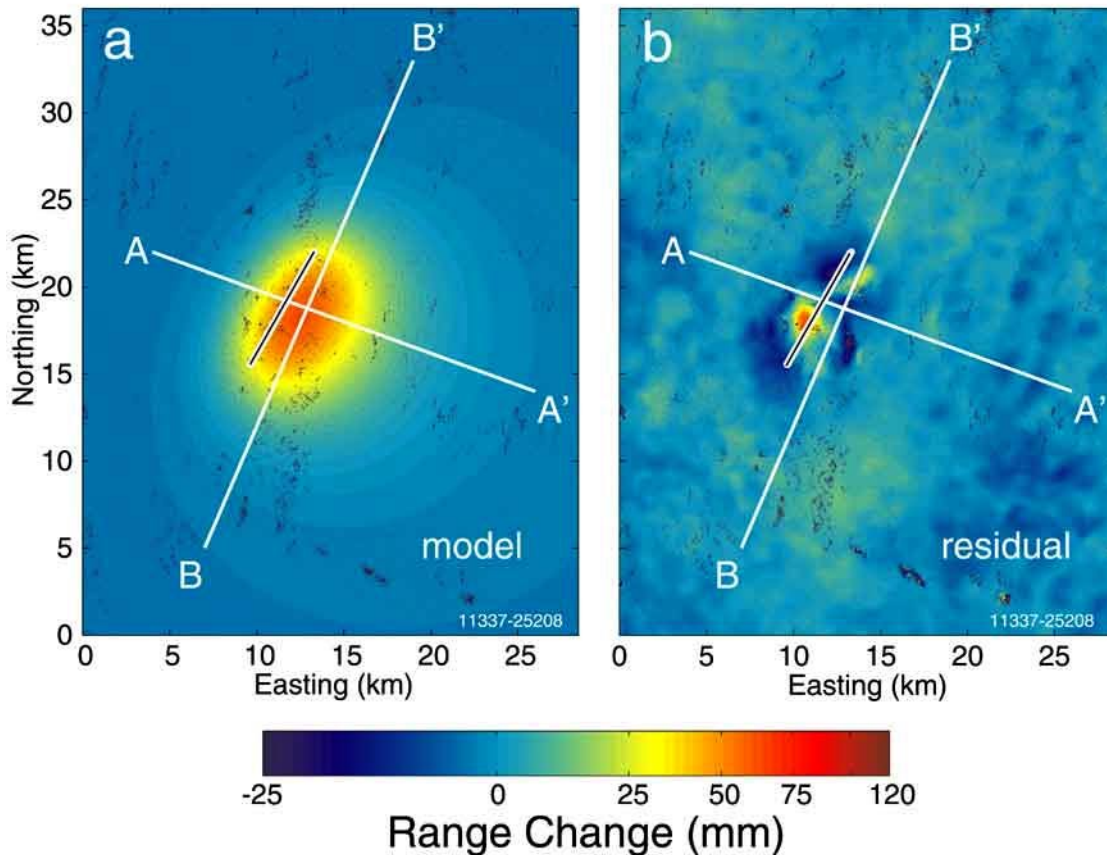

Figure 6 Best fit elastic dislocation model for data shown in Figure 4a. The 7.4 km black on white line , sub-parallel to B-B just west of the intersection of the two profiles, is the surface projection of the best fit dislocation model. The color scale on the bottom shows the amount of range change associated with the colors. **(a)** Synthetic interferogram generated using the parameters in Table 2. **(b**) residual interferogram formed by subtracting the range change values shown in Figure 6a from those shown in Figure 4a.

The dislocation models are similar for each of the five inversions in that the dislocation source reduces to a north-northeast striking very narrow collapsing lath shaped body. Table 2 lists the parameters of the best-fit models derived from the interferograms in Figure 4, which on average account for ~90 % of the observed signal. Because the parameters of width and contraction for the dislocation are highly dependent, we have listed the product of the two parameters in Table 2. The errors are minimized with very narrow width values of ~50 m with corresponding contraction of ~12 m. At the 95% confidence level, widths of ~2.2 km with corresponding contraction of ~0.3 m are allowable. The product of width and amount of contraction at the 95% limit are slightly changed relative to the best fit values, because of a weak dependence of the product on depth.

Figure No.	Center Location		Strike (° Az)	Depth (km)	East Dip (°)	Length (km)	$w \times u_3$ (m^2)	w and u_3 at 10 MPa	
	X_0 (km)	Y_0 (km)						w (km)	u_3 (m)
4a	11.4	18.8	210	4.6	20	7.4	635	1.4	0.46
4b	10.4	21.2	208	4.7	50	8.9	808	1.6	0.51
4c	10.0	19.4	197	3.9	61	7.6	911	1.6	0.57
4d	11.2	19.9	211	4.0	30	8.0	853	1.5	0.51
4e	12.5	21.1	203	3.6	32	8.7	754	1.5	0.50

Table 2. Columns 1-7 are model parameters of best fit elastic dislocation source (sill) for each of the interferograms in Figure 4. The coordinates listed in columns three and four are the center of the sill locations for the best fit for each interferogram. Column eight is the product of sill width (w) and contraction (u_3). Columns nine and ten are the width and contraction of the best fit sill forcing the stress drop to be 10 MPa.

Although the optimized model favors narrow widths, the corresponding amount of contraction leads to unreasonably large stress drops of ~ 3 GPa. To make a viable estimate of the amount of contraction and width, we assume a range of reasonable stress drops of 10 — 100 MPa. From this range of stress drops we calculate respective ranges of width to be from 1.5 km to 0.4 km, and amount of contraction to be from 0.4 to 1.6 m for the dislocation sources. The dislocation model, equivalent to a single fracture surface, should only be considered to be a simple representation of a more complex system. The true source is more likely a composite source that consists of a system of fractures.

The depths of the laths range from 3.1 to 4.7 km and the depths of Mogi sources modeled to fit the interferograms in Figure 4 range from 3.1 to 4.2 km. The modeled interferograms are all from descending orbits, but we have also modeled one intererogram from an ascending pair of orbits from 1992 to 1996. The best fit dislocation model is similar to those found for the ascending orbits: dipping shallowly to the east, striking about 10° east of north, and at ~ 5 km depth. Fialko and Simons (2000) modeled the deformation field inferred from satellite interferometry, using multiple prolate spheroidal sources. The largest of their sources, for the two interferograms they modeled (one of which is common to our Figure 3a), is about 6.6 km in maximum dimension, striking just east of north at a depth of ~3 km, similar but shallower than our sources. The errors in the remaining parameters for the dislocation model are small in individual models and are best assessed using the spread of values shown in Table 2. The strike of the dislocation is perpendicular to the least compressive stress direction inferred from geologic, seismologic and geodetic data (*Weaver and Hill,* 1979; *Bacon et al.*, 1980; *Gan et al.,* 2000).

Discussion and Conclusions

In seismically active areas the brittle-ductile transition is thought to fall between the depth of peak seismicity and the depth of deepest seismicity, which is between the depths of 3 and 6 km beneath the Coso geothermal field. *Walter and Weaver* (1980) showed that seismicity in an area including the geothermal field (before geothermal production began) was sharply peaked at ~5 km depth, with a steep decline in seismicity at greater depth. Their seismicity cross-sections revealed the seismicity to be generally shallower than 5 km in what is now the geothermal area. *Feng and Lees* (1998) showed that seismicity beneath the geothermal area is generally shallower than ~4 km. They suggested that this represented a shallowing of the brittle-ductile transition beneath the geothermal field brought about by raised isotherms beneath the field. More than ten years (1990-2000) of high-resolution microseismic data from the 16 station Coso network show that the lower limit of the seismogenic zone beneath the production area is near 6 km depth. The highest temperature measured in the geothermal production wells is 340 °C at a depth of ~2.5 km in the south end of the geothermal field (*Moore et al.,* 1989),

independently suggesting that the temperature near 4 km depth may be high enough to lead to ductile deformation.

Reasenberg et al.(1980) inferred a body with anomalously low P-wave velocity beneath the Coso geothermal area that probably corresponds to the rhyolite magma body that is the source of heat for the field. *Reasenberg et al.* used telseismic tomography to delineate a low velocity zone from 5 to 20 km depth, about 5 km wide at the top and increasingly elongate with increasing depth in the N 25°E direction. This body corresponds closely to the location of the anomalous deformation signal shown in Figs. 3 and 4. Its depth agrees well with the depth of the parent magma body inferred from a study of the rhyolite domes and flows erupted in the last ~0.3 Ma (*Manley and Bacon,* 2000). This study used phenocryst thermobarometry to infer that the depth to the top of the rhyolite magma reservoir during the last eruption ~0.04 million years ago was ~5.5 km.

The equivalent dislocation sources we use to model the deformation appear to be aligned with the seismologically and geologically inferred magma bodies and to the direction of maximum compressive stress field in the Coso Range. The average depth of the sources, ~ 4 km, is at or above the inferred top of the parent magma body and very close to the depth of the brittle ductile transition derived from seismicity. The orientation of the modeled sources is consistent with closure of a system of pressurized cracks striking perpendicular to the direction of the least compressive stress.

Based on these associations we propose that the long-wavelength component of the deformation field we have measured and modeled results from leakage of magmatic fluids through a self-sealed zone at the base of the brittle-ductile transition and above a crystallizing body of rhyolite. This inference, based on a model proposed by Fournier (1999), effectively extends the idea of *Bacon s* (1982) tectonically leaking magmatic system to the overlying hydrothermal system. In Fournier s model horizontal lenses of hypersaline brine and gas exsolved from the crystallizing rhyolite accumulate above the magma body but below the brittle-ductile transition. Central to Fournier s model is the evidence that crustal rocks, such as the granitic host for the Coso geothermal field, can deform as a plastic in the depth range of 2-6 km surrounding intrusions of magma. The temperatures required for plastic behavior of the crustal rocks are > 400…C, at strain rates

of ~10^{-14} sec^{-1} (Fournier, 1999). A narrow self-sealed zone forms at the brittle-ductile transition by a decrease in permeability brought about by plastic flow and precipitation of minerals at the contact between the meteoric fluids circulating in the brittle rock (above) and the magmatic fluids (below). When the zone is sealed, the brine-gas reservoir is pressurized and surface uplift results. Thinning of the brittle rock above the magma body (most likely from extension in Coso) could lead to breaches in the self-sealing zone and movement of magmatic fluids into the region of circulating meteoric fluids. The resulting depressurization of the brine-gas reservoir would then produce surface subsidence.

Breaching of the self-sealed zone may be episodic, leading to cycles of uplift and subsidence like those observed at Yellowstone caldera (*Wicks et al.,* 1998). Although the deformation history of the Coso Range is limited, there is evidence suggesting similar behavior. *Savage* (*unpublished report,* 1982) conducted a study of the Coso geothermal area that measured deformation accumulated before geothermal production began. Vertical deformation was measured between 1975 and 1982 on a 20-km-long leveling line running from Red Hill to Coso Hot Springs (Figure 2). The segment of the leveling line between Sugar Loaf Mountain and Coso Hot Springs (Figure 2) experienced ~30 mm of uplift relative to Red Hill in the seven year time span covered. The area of relative uplift corresponds to one of the local peaks of range change (subsidence) in the interferograms in Figs. 3 and 4. This change in signature from uplift to subsidence could be interpreted as the formation of a breach in the self-sealed zone, or it could simply be due to the initiation of subsidence related to the onset of geothermal production.

Although we favor a source at ~4 km depth and the model of *Fournier* (1999) to explain the long wavelength deformation at Coso, we cannot eliminate the possibility that the deformation signal we have modeled results from a superposition of shallow sources. However, the long wavelength signal is quite smooth (see Figures 3 and 7) and it seems unlikely that shallow sources would be fortuitously distributed in just the way required to explain this long wavelength signal. The steady-state nature of the long wavelength deformation (Figure 4) also argues against a shallow, production-related origin, since the observed local rates of deformation from these sources is non-uniform. Thus we suggest that the smoothness of the signal results from upward continuation of a deformation source at depth.
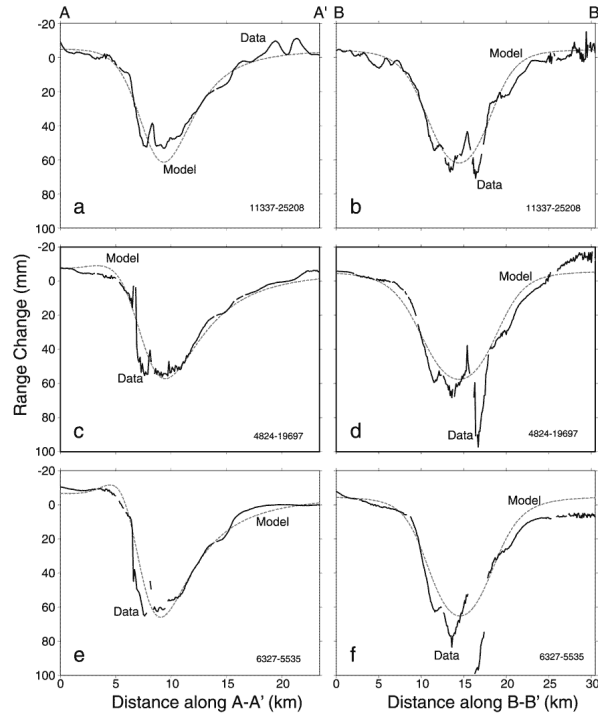
Figure 7 Detailed comparisons of model-predicted range change (Table 2) and observed range change (Figure 4) for three interferograms without a common scene. The plots on the left show the comparison for values along A-A and the plots on the right show the comparison for values along B-B . **(a) & (b)** Orbit pair 11337-25208, 93/09/15 — 96/05/10.**(c) & (d)** Orbit pair 4824-19697, 92/06/17-95/04/21. **(e) & (f)** Orbit pair 6327-5535, 92/09/30-96/05/11.

One additional line of evidence supports a deep source for hydrothermal fluids and deformation in the Coso geothermal field. *Moore et al.* (1989) analyzed the chemistry of fluids produced from the wells in the field and fluid inclusions in cores taken during drilling of wells to construct a fluid flow model for the field. They proposed that the source of the field is a plume of hot fluid that originates deep beneath the southern end of the field and spreads to shallower depths in the north and east sides of the field. We suggest that this plume may originate at the brittle-ductile transition, tapping a reservoir of magmatic fluids as envisioned in the model of *Fournier* (1999).

Acknowledgements

References

Bacon, C. R. Time-predictable bimodal volcanism in the Coso Range, California, *Geology*, 10, 65-69, 1982

Bacon, C. R., Duffield, W. A. and Nakamura, K., Distribution of Quaternary rhyolite domes of the Coso Range, California: Implications for extent of the geothermal anomaly, *J. Geophys. Res.*, 85, 2425-2433, 1980.

Duffield, W. A. and C. R. Bacon, Geologic map of the Coso Volcanic Field and adjacent areas, Inyo County, California, U. S. Geol. Surv. Misc. Geol. Inv. Map I-1200, 1981.

Duffield, W. A., C. R. Bacon and G. B. Dalrymple, Late Cenozoic volcanism, geochronology, and structure of the Coso Range, Inyo County, California, *J. Geophys. Res.*, 85, 2381-2404, 1980.

Feigl, K. and E. Dupr , RNGCHN: A program to calculate displacement components from dislocations in an elastic half-space with applications for modeling geodetic measurements of crustal deformation, *Comp. and Geosci.*, 25, 695-704. 1999.

Feng, Q. and J. M. Lees, Microseismicity, stress, and fracture in the Coso Geothermal Field, California, *Tectonophysics* 289, 221-238, 1998.

Fialko, Y., and M. Simons, Deformation and seismicity in the Coso geothermal area, Inyo County, California: Observations and modeling using satellite radar interferometry, *J. Geophys. Res.*, 105, 21781-21793, 2000.

Fournier, R. O., Hydrothermal processes related to movement of fluid from plastic into brittle rock in the magmatic-epithermal environment, *Econ. Geol. and Bull. Soc. Econ. Geol.*, 94, 1193-1211, 1999.

Gan, W., J. L. Svarc, J. C., Savage and W. H. Prescott, Strain accumulation across the eastern California shear zone at latitude 36¡30'N, *J. Geophys. Res*., 105, 16229-16236, 2000.

Goldstein, R. M. and C. L. Werner, Radar interferogram filtering for geophysical applications, *Geophys. Res. Lett.*, 25, 4035-4038, 1998

Goldstein, R. M., H. A. Zebker and C. L. Werner, Satellite radar interferometry: two-dimensional phase unwrapping, *Radio. Sci.,* 23, 713-720, 1988.

Haukkson, E., 3-D earthquake locations in southern California, *J. Geophys. Res*., 105, 13875-13903, 2000.

Hearn, E. H. and E. D. Humphreys, Kinematics of the southern Walker Lane Belt and motion of the Sierra Nevada block, California, *J. Geophys. Res.*, 103, 27033-27049, 1998.

Jennings, C. W., compiler, Fault map of California with locations of volcanoes, thermal springs, and thermal wells, Cal. Div. Of Mines and Geol. Geologic Data Map 1, 1975

King, R. W., S. C. McClusky and B. H. Hager, Reduction and utilization of GPS data from the Navy Geothermal Crustal Motion Survey Network, progress report for the period 9 September 1997 — 30 September 1998, submitted to the Naval Air Weapons Center, 1998.

Malin, P. E., The seismicity of extensional hydrothermal systems, *Geotherm. Res. Council Trans.*, 18, 17-22, 1994.

Manley, C. R. and C. R. Bacon, Rhyolite Thermobarometry and the shallowing of the magma reservoir, Coso Volcanic Field, California, J. Petrol. 41, 149-174, 2000.

Massonnet, D.,P. Briole and A. Arnaud, Deflation of Mt. Etna monitored by spaceborne interferometry, *Nature* 375, 567-570, 1995.

Mogi, K., Relations between the eruptions of various volcanoes and the deformations of the ground surface around them, *Bull. Earthquake Res. Inst. Univ. Tokyo*, **36**, 99-134, 1958.

Monastero, F. C., A. M. Katzenstein, A. F. Glazner, J. S. Miller, M. Adams and M. A. Hasting, Evidence for a nascent metamorphic core complex at the Coso geothermal area, California, *EOS, Trans. AGU*, 78, F659, 1997

Moore, J. N., M. C. Adams, B. P. Bishop and P. Hirtz, A fluid flow model of the Coso geothermal system: Data from production fluids and fluid inclusions*, Proc. 14th*

Workshop on Geotherm. Res. Eng., Stanford Univ., Jan. 24-26, 140-144, 1989.

Novak, S. W. and C. R. Bacon, Pliocene volcanic rocks of the Coso Range, Inyo County, California, *U. S. Geol. Surv. Prof. Pap.* 1383, 43pp, 1986.

Okada, Y., Surface deformation due to shear and tensile faults in a half-space*, Bull. Seis. Soc. Am.*, 75, 1135-1154, 1985.

Reasenberg, P.,W. Ellsworth and A. Walter, Teleseismic evidence for a low-velocity body under the Coso geothermal area, *J. Geophys. Res*. 85, 2471-2483, 1980.

Saunders, C., P. Ho-Liu, D. Rinn and H. Kanamori, Anomalous shear wave attenuation in the shallow crust beneath the Coso volcanic region, California, J. Geophys. Res., 93, 3321-3338, 1988.

Walck, M. C. and R. W. Clayton, *P* wave velocity variations in the Coso region, California, derived from local earthquake travel times, *J. Geophys. Res.* 92, 393-405, 1987.

Walter, A. and C. S. Weaver, Seismicity of the Coso Range, California*, J. Geophys. Re*s., 85, 2441-2458, 1980.

Weaver, C. S. and D. P. Hill, Earthquake swarms and local crustal spreading along major strike-slip faults in California, *Pure Appl. Geophys.*, 117, 51-64, 1979.

Wessel, P. and W. Smith, New version of Generic Mapping Tools (GMT) released, *EOS Trans. AGU*, 76, 329, 1995.

Wicks, C. Jr., W. Thatcher and D. Dzurisin, Migration of fluids beneath Yellowstone Caldera inferred from satellite radar interferometry, *Science*, 282, 458-462, 1998.

Wu, H. and J. M. Lees, Attenuation structure of Coso geothermal area, California, from wave pulse widths, *Bull. Seis. Soc. Am.*, 86, 1574-1590, 1996.